J. Phys. Chem. B **2005,** *109,* 10835−10841

A Comparative Study of Unrelaxed Surfaces on Quartz and Kaolinite, Using the Periodic Density Functional Theory

Vladimir V. Murashov* and Eugene Demchuk†

Health Effects Laboratory Division, National Institute for Occupational Safety and Health, Centers for Disease Control and Prevention, Morgantown, West Virginia 26505

Received: January 7, 2005; In Final Form: March 11, 2005

To investigate surface properties of fractured silica particles, which are commonly connected to the etiology of silica toxicity, models of low-index unrelaxed surfaces of quartz and kaolinite were constructed and analyzed using the periodic density functional theory calculations. The models were used to investigate surface sites that emerge in the processes of heterolytic and homolytic cleavage of quartz. It is found that the quartz surface is stabilized by two types of interactions. One, due to a more even charge distribution of sites, was characterized by surface energies of up to 0.025 eV·Å^{-2} and the other, due to a more even oxygen distribution between complementary surfaces, was up to 0.036 eV·Å^{-2}. The total specific surface energies of unrelaxed surfaces ranged from 0.161 to 0.200 eV·Å^{-2} for quartz and from 0.017 to 0.158 eV·Å^{-2} for kaolinite. For the conchoidal fracture of quartz an average specific surface energy of 0.187 eV·Å^{-2} was obtained. These results provide a foundation for further characterization of the surface properties of mechanically comminuted respirable silica particulate and for reduction of occupational health hazards due to pulverized silica.

Introduction

Pulverized respirable crystalline silica, a common byproduct of mining, construction, and various manufacturing processes, is a major occupational hazard causing an increased risk of pulmonary fibrosis and pneumoconiosis (silicosis), and lung cancer.[1] The biological toxicity and pathogenicity of silica is attributed to the presence of surface silanol groups.[2] To comprehensively characterize the toxicity of silica/silicate mineral dust, information about the type and density of surface sites must be available. In this work we develop atomistic models of unrelaxed quartz and kaolinite surfaces, and use these models to study the process of fracture and to characterize fractured material.

Although a problem of fracture development in brittle single crystals has been addressed in the literature, there is no clear consensus about criteria determining the cleavage planes. Several factors including fracture toughness, charge effects, bond density, elastic modulus and surface energy have been considered as determinants shaping the fragments of mechanically comminuted crystals. In the present series we view this problem from the perspective of statistical analysis. It was found that in crystalline silica polymorphs (all of which lack distinguished crystallographic planes of weakness) the energy of *unrelaxed* surface is characteristic of cleavage faceting. Previous efforts relevant to the topic of current discussion include the structural analysis of unrelaxed surfaces carried out for a limited number of crystallographic planes of quartz[3] and periodic density functional theory (DFT) calculations which have been performed on (1) silica bulk[4] and unrelaxed (100) and (001) surfaces of quartz,[5] and (2) crystalline kaolinite bulk[6,7] and the (001) surface of silica−alumina bilayers.[8] In the present work we further developed atomistic models of unrelaxed quartz and kaolinite surfaces, which encompass a representative pool of crystallographic planes, and used them to study the process of fracture and to structurally characterize the surface of fractured material. For all studied surfaces we also calculated the associated surface energies, which were further used to estimate silanol densities in silica/silicate particulate.[9] These calculations were carried out on periodic systems with DFT methods.

Materials and Methods

Selection of Quartz Surfaces. Quartz is a tetrahedral silica polymorph, whose structure can be viewed as a network of corner-linked silica tetrahedra (Figure 1a). Unlike many brittle crystals, α-quartz does not possess perfect crystallographic planes of cleavage.[10] Instead, an application of external stress to single quartz crystals reveals a large number of cleavage planes with rather poorly defined individual preferences. In this sense the fracture of quartz resembles that of amorphous materials, which is commonly referred to as the *conchoidal fracture*. At the microscopic level the irregular conchoidal fracture of quartz is made up of terraces of cleavage planes, which follow specific probabilities. Bloss and Gibbs derived the statistics of quartz cleavage planes experimentally using a sufficiently large number of fractured grains of clear synthetic quartz.[11] In their study a distribution of crystallographic surfaces on fractured α-quartz was constructed by using optical measurements on 7573 faces of quartz grains, the observed singular surfaces were classified, and the associated frequencies of cleavage plane occurrences were estimated. Due to experimental setup limitations, the presence of the {001} form in the sample could be determined qualitatively but not quantitatively. Also, the correlated forms of quartz could not be distinguished and were appropriately grouped together. Bloss and Gibbs identified 18 crystal forms, which were categorized into 8 groups (Table 1, supplemented with the (001) surface). This set of forms represents a greater diversity of termination planes than on grown crystals. The latter is limited to only the 6 most common

---

* Address correspondence to this author at the National Institute for Occupational Safety and Health, 200 Independence Ave., Room 733“G”, Washington, DC 20201. E-mail: vmurashov@cdc.gov.

† Adjunct faculty member at the School of Pharmacy, West Virginia University, Morgantown, West Virginia 26506.

10.1021/jp050113a Published 2005 by the American Chemical Society

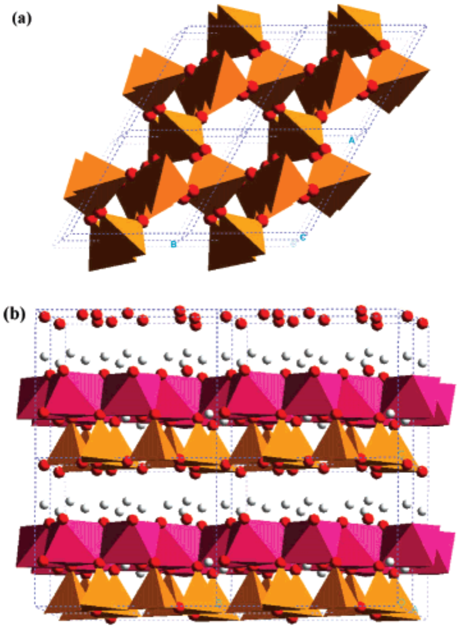

Figure 1. Polyhedral representation of atomic structures of (a) quartz and (b) kaolinite. White spheres represent hydrogen atoms, red spheres represent oxygen atoms, orange spheres represent silicon atoms, and purple spheres represent aluminum atoms.

crystal forms, including the first-order hexagonal prism {100}, positive {101} and negative {011} rhombohedra, trigonal pyramid {111}, positive trigonal trapezohedron {511}, and right trigonal prism {110} (Figure 2a). We developed computer models for surfaces of these and the remaining 12 crystal forms reported by Bloss and Gibbs,[12] and used them for physical–chemical characterization of the fractured quartz surface (described below).

Selection of Kaolinite Surfaces. Kaolinite belongs to a group of phyllosilicate minerals. It is rarely found in the form of macroscopic crystals but commonly as thin platy stacked clusters of pseudohexagonal sheets aggregated into compact clay-like masses. The ideal structure of kaolinite can be viewed as a combination of gibbsite dioctahedral and silica tetrahedral layers, in which the silica tetrahedra substitute for the exterior hydroxyl groups on one side of the gibbsite layer.[13] A single layer of silica tetrahedra is connected by common apex oxygen atoms to a single layer of alumina octahedra, thus making a 1:1 phyllosilicate (Figure 1b). The layers are bonded together by only weak interatomic forces, often by hydrogen bonding from water. Therefore, a plane parallel to the bilayers is distinguished as a perfect and the only cleavage plane in kaolinite.[14] This cleavage plane corresponds to the basal {001} face of the mineral. The natural habit of kaolinite, described as the hexagonal or rhombic plate (Figure 2b), includes the basal {001} and side {010} and {110} pseudoparallelohedra.[15,16] Generally, due to a higher density of gibbsite layers, which are composed of closed-packed oxygen atoms, the gibbsite layers direct the microcrystal morphology of kaolinite. The morphology of gibbsite crystals is pseudohexagonal with the most commonly occurring {001}, {010}, {100}, {101}, {110}, and {112} forms.[17−19] As described below, we modeled surfaces belonging to these six forms, along with {011} and {111} forms, which were included for generality (Table 2).

TABLE 1: Surface Energies and Sites in Periodic Spin-Paired Calculations of Quartz

type[a]	sites on complementary surfaces	$-E_{\mathrm{slab}}$ [eV]	γ_{fr} [eV·Å^{-2}]
(101)	$2Q^3(O)/2Q^3$	273.2966	0.187
	$Q^3(O) + Q^3/Q^3(O) + Q^3$	275.0290	0.162
(011)	$2Q^3(O)/2Q^3$	273.4686	0.184
	$Q^3(O) + Q^3/Q^3(O) + Q^3$	274.8357	0.165
(112)	$3Q^3(O) + Q^3/Q^3(O) + 3Q^3$	262.3980	0.184
	$2Q^3(O) + 2Q^3/2Q^3(O) + 2Q^3$	263.1183	0.179
$(2\bar{1}2)$	$3Q^3(O) + Q^3/Q^3(O) + 3Q^3$	262.3994	0.184
	$2Q^3(O) + 2Q^3/2Q^3(O) + 2Q^3$	263.1131	0.179
(001)	$Q^2/Q^2(O)_2$	133.1841	0.229
	$Q^2(O)/Q^2(O)$	134.7799	0.193
(102)	$Q^2 + 2Q^3/Q^2(O)_2 + 2Q^3(O)$	263.4357	0.221
	$Q^2(O) + Q^3 + Q^3(O)/$ $Q^2(O) + Q^3(O) + Q^3$	265.8482	0.198
(012)	$Q^2 + 2Q^3/Q^2(O)_2 + 2Q^3(O)$	263.3765	0.222
	$Q^2(O) + Q^3 + Q^3(O)/$ $Q^2(O) + Q^3(O) + Q^3$	265.7101	0.200
(100)	$Q^2/2Q^3(O)$	276.2237	0.185
	$Q^2(O)/Q^3(O) + Q^3$	276.7203	0.177
(111)	$Q^2 + 2Q^3/Q^2(O)_2 + 2Q^3(O)$	263.4036	0.217
	$Q^2(O) + 2Q^3/Q^2(O)_2 + Q^3(O)+ Q^3$	264.1175	0.211
	$Q^2(O) + 2Q^3/Q^2(O) + 2Q^3(O)$	264.8049	0.204
	$Q^2(O) + Q^3(O) + Q^3/$ $Q^2(O) + Q^3(O) + Q^3$	265.7807	0.195
$(2\bar{1}1)$	$Q^2 + 2Q^3/Q^2(O)_2 + 2Q^3(O)$	263.4887	0.216
	$Q^2(O) + 2Q^3 /Q^2(O)_2 + Q^3(O)+ Q^3$	264.1164	0.211
	$Q^2(O) + 2Q^3/Q^2(O) + 2Q^3(O)$	264.9711	0.203
	$Q^2(O) + Q^3(O)+ Q^3/$ $Q^2(O) + Q^3(O)+ Q^3$	265.9828	0.193
(110)	$2Q^2(O)/Q^2 + 2Q^3(O)$	267.4363	0.197
	$2Q^2(O)/Q^2(O) + Q^3(O) + Q^3$	267.4595	0.197
$(2\bar{1}0)$	$2Q^2(O)/Q^2 + 2Q^3(O)$	267.3379	0.198
	$2Q^2(O)/Q^2(O) + Q^3(O) + Q^3$	267.6614	0.195
(302)	$3Q^3(O) + 3Q^3/Q^2 + 3Q^3(O) + Q^3$	537.9521	0.185
(032)	$3Q^3(O) + 3Q^3/Q^2 + 3Q^3(O) + Q^3$	537.5856	0.187
(511)	$4Q^2(O) + Q^2 + 2Q^3(O)/$ $3Q^2(O) + 3Q^3(O) + 3Q^3$	753.2694	0.186

[a] Correlated crystal forms are separated by a space.

Computational Details. A notation for silica surface sites in this text is adopted from the de facto standard Nuclear Magnetic Resonance classification, in which the surface site Q^n is classified by the number of attached silica units, n. In this notation Q^0 represents a silicon atom that is not connected to any other silica units (e.g. orthosilicic acid); Q^1 represents a silicon atom connected to another silica unit; and so on up to Q,[4] which represents a silicon atom that is connected to four silica units, i.e. similar to silicon atoms in bulk quartz. The description of surface termination of the unit Q suffixes the notation of surface site. For example, a surface geminal silanol site can be classified as $Q^2(OH)_2$ and a siloxane site on the (001) surface of kaolinite can be described as $Q^3(OAl_2)$. By analogy, aluminum atoms bonded to n tricoordinated oxygen atoms (as in bulk kaolinite) are designated as A^n. If an oxygen ligand has other coordination numbers, then this ligand is added as a suffix description. For example, an aluminum atom bonded to three tricoordinated oxygen atoms of gibbsite and a dicoordinated oxygen atom, which in its turn is bonded to a hydrogen atom, is denoted as $A^3(OH)$. While the electronic structure of relaxed pristine silica surface sites has been described earlier,[20,21] the distribution of nonbonding valence electrons around unrelaxed surface sites may be ambiguous and therefore in the present work the attribution of surface sites is carried out without the assignment of formal charges and unpaired electrons. Hence, sites considered are designated as $Q^3(O)$, Q^3, Q^2, $Q^2(O)_2$, and $Q^2(O)$. Figure 3 illustrates the location of surface sites on the (511) surface of quartz and on the (010) surface of kaolinite. Upon hydroxylation Q^3 sites turn into single silanol $Q^3(OH)$

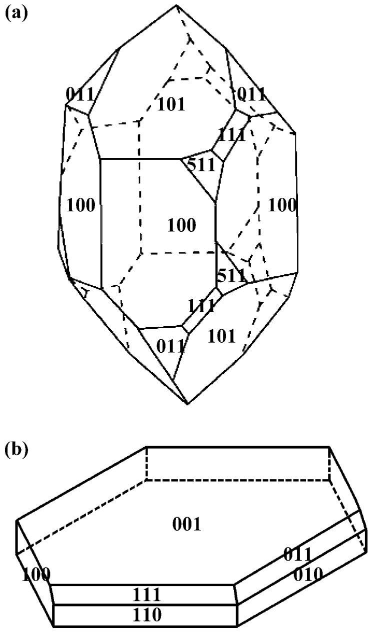

Figure 2. Common habits of natural (a) quartz and (b) kaolinite crystals. Numbers indicate crystal forms. The thickness of the kaolinite crystal is exaggerated for clarity.

sites, while Q^2 sites turn into geminal silanol $Q^2(OH)_2$ sites (exposure of fractured silica surface to water vapors with partial pressure higher than 1.33×10^{-7} Pa results in the hydrolysis of surface sites and formation of silanol groups, which is completed within 1 h[22]). This is why we term Q^3 as "single" and Q^2 as "geminal" sites.

Periodic boundary DFT calculations with a plane-wave basis set and the projector-augmented wave (PAW) method[23-25] were performed with use of the VASP code.[26,27] Since this study was focused on the energies rather than accurate structural parameters, we employed the generalized gradient approximation (GGA) to the exchange-correlation functional, which is parametrized according to Perdew−Wang.[28] This method yields better relative energies of quartz polymorphs[4] and, therefore, it is better suited for studying the energy differences between quartz surfaces. The energy cutoff for the plane-wave basis set was set to 500 eV[6] to ensure a high precision of energy calculations of silica/alumina slabs. The Brillouin zone was sampled by using the Monkhorst−Pack technique[29] with the 3 × 3 × 1 k-points mesh for slabs (this choice of k-point mesh is justified by the large supercells employed in this study)[6,30] and 2 × 4 × 4 (quartz in orthorhombic setting) and 3 × 3 × 3 (kaolinite) k-point meshes for bulk crystals. The integration was performed with use of the tetrahedron method[31] with Blöchl corrections.[23]

Initially, the minimum-energy density of bulk quartz was established by a set of fixed volume energy-minimization calculations on supercells of the structurally left-handed enantiomorph of α-quartz (the $P3_221$ space-group symmetry) with a positive tilt angle of silica tetrahedra around the x axis. Relaxation of ions to the minimum energy state was performed with a conjugate gradient algorithm. The optimization was terminated when the estimated total energy convergence achieved 10^{-4} eV for both the electronic and ionic (in bulk calculations) minimizations. Since this study does not focus on finding fine structural parameters of bulk quartz, we optimized bulk density with respect to only the scaling parameter: to change the cell volume, the unit cell parameters were scaled, while directional cosines were kept fixed. This protocol resulted in the following unit cell parameters (the experimental values[32] are given in parentheses): $a = 5.057$ Å (4.9160 Å) and $c = 5.564$ Å (5.4054 Å), which are about 3% larger than the experimental numbers and agree well with previous DFT calculations.[4] In the optimized structure of quartz, Si−O−Si angles converged at 149.9° (143.7°), pairs of Si−O−Si−O torsion angles at 46.2°/115.8° (31.1°/131.4°) and −3.4°/−73.6° (15.8°/−93.3°), Si−O bond lengths, which are unequal in the silica tetrahedron, at 1.625 Å (1.6046 Å) and 1.627 Å (1.6137 Å), and the tilt angle at 10.0° (16.3°).

The space group symmetry of kaolinite is $P1$.[33] Similar to quartz, the unit cell volume was changed by scaling all unit cell parameters by the same factor, while the unit cell angles were kept at the experimental values of $\alpha = 91.93°$, $\beta = 105.04°$, and $\gamma = 89.79°$. Large unit cell size and a high number of variables prevented us from full structural optimization. Earlier calculations focused on structural features of bulk kaolinite kept unit cell parameters frozen at experimental values.[6] In the calculations of kaolinite the minimum energy state was achieved with unit cell parameters 1% larger than the experimentally determined numbers.[33] They were $a = 5.200$ Å (5.149 Å), $b = 9.023$ (8.934 Å), $c = 7.458$ Å (7.384 Å).

The optimized bulk structures were used to construct slabs along the cleavage planes with desired Miller indices. The slabs with atomic nuclei frozen in positions obtained for optimized bulk structures were used in surface energy calculations with the periodic boundary conditions employed. This type of calculation with frozen nuclei was used to test the likelihood of existence of hypothetical nascent surfaces (the calculated energies were further used to derive the probability of surface formation;[9] they are not appropriate for characterization of relaxed surfaces, which are described in a separate publication).[21] The calculations were carried out on sandwich-like supercells consisting of the slab and a vacuum layer, which separated the slab from its neighboring periodic-boundary image. The slab was 9 to 10 Å thick, which was shown to be enough to study structural relaxation of quartz[30] and, therefore, is sufficient to study unrelaxed surfaces. The vacuum layer was 10 Å thick. This level of interslab separation was adopted based on a series of test calculations on the (001) surface of quartz. In the tests, the convergence of slab energy with respect to the interslab separation was achieved already at 10 Å, and further increase of the separation layer up to 20 Å altered the total slab energy by only 3.5×10^{-4} eV or (3×10^{-4})% at most.

When appropriate, several cuts were prepared for the same Miller index by varying the position and thickness of the slab within bulk quartz. Since complementary surfaces on the opposite sides of the slab are generally different, the surface energies reported in Tables 1 through 3 incorporate both. The specific energies of unrelaxed surfaces were calculated as $\gamma_{\mathrm{fr}} = (E_{\mathrm{slab}} - nE_{\mathrm{bulk}})/S$, where E_{bulk} is the energy of the slab molecular units in bulk, n is the number of molecular units in the slab supercell, and S is the total surface area formed in cleavage. For the SiO_2 molecular units E_{bulk} was −23.8883 eV and $n = 12$ [except for the slab of the (001) surface, when $n = 6$, the slab of the (511) surface, when $n = 34$, and the slabs of the (302) and (032) surfaces, when $n = 24$]. For the $Si_2Al_2O_5(OH)_4$ molecular units E_{bulk} was −115.4499 eV and $n = 4$.

Results and Discussion

Quartz Surfaces. As a rule, crystal cleavage results in the formation of two nonidentical complementary surfaces (unless the cleavage plane contains elements of symmetry such as the center of inversion or 2-fold axis). The distinctions are determined by the crystal structure and the way the bond

TABLE 2: Surface Energies and Sites in Periodic Calculations of Kaolinite

system	sites on complementary surfaces	$-E_{\mathrm{slab}}$ [eV]	γ_{fr} [eV·Å^{-2}]
(001)	$8Q^3(\mathrm{OAl_2})/8A^6$	458.5628	0.017
(100)	$Q^2(\mathrm{OAl_2}) + Q^2(\mathrm{OAl}) + A^4(\mathrm{OH})_2 + A^4(\mathrm{OH})(\mathrm{OSi})/2Q^2(\mathrm{O})(\mathrm{OAl_2}) + 2A^4$	440.5987	0.158
	$Q^2(\mathrm{OAl}) + Q^2(\mathrm{O})(\mathrm{OAl_2}) + A^4(\mathrm{OH})_2 + A^4(\mathrm{OH})(\mathrm{OSi})/Q^2(\mathrm{OAl_2}) + Q^2(\mathrm{O})(\mathrm{OAl_2}) + 2A^4$	438.7779	0.171
(010)	$2Q^2(\mathrm{OAl}) + 2A^4(\mathrm{OH})(\mathrm{OSi})/2Q^2(\mathrm{O})(\mathrm{OAl_2}) + 2A^4$	442.2333	0.131
	$2Q^1(\mathrm{O})(\mathrm{OAl_2}) + 2A^4(\mathrm{OH})/2Q^1(\mathrm{O})(\mathrm{OAl}) + 2A^4(\mathrm{OSi})$	439.0239	0.152
(110)	$2Q^2(\mathrm{OAl}) + 2A^4(\mathrm{OH})(\mathrm{OSi})/2Q^2(\mathrm{O})(\mathrm{OAl_2}) + 2A^4$	441.6383	0.131
	$2Q^1(\mathrm{O})(\mathrm{OAl_2}) + 2A^4(\mathrm{OH})/2Q^1(\mathrm{O})(\mathrm{OAl}) + 2A^4(\mathrm{OSi})$	439.4372	0.145
(101)	$2Q^2(\mathrm{OAl_2}) + 2A^3(\mathrm{OH})/Q^2(\mathrm{O})_2 + Q^2(\mathrm{O})(\mathrm{OAl}) + A^4(\mathrm{OSi}) + A^4(\mathrm{OH})$	438.2084	0.129
	$Q^2(\mathrm{OAl_2}) + Q^2(\mathrm{O})(\mathrm{OAl_2}) + 2A^3(\mathrm{OH})/Q^2(\mathrm{O}) + Q^2(\mathrm{O})(\mathrm{OAl}) + A^4(\mathrm{OSi}) + A^4(\mathrm{OH})$	439.5145	0.122
(011)	$Q^2(\mathrm{OAl_2}) + A^5 + A^3(\mathrm{OH})/Q^2(\mathrm{O})_2 + Q^3(\mathrm{OAl}) + A^4(\mathrm{OSi})$	447.4967	0.117
	$Q^2(\mathrm{O})(\mathrm{OAl_2}) + A^5 + A^3(\mathrm{OH})/Q^2(\mathrm{O}) + Q^3(\mathrm{OAl}) + A^4(\mathrm{OSi})$	447.6719	0.116
(111)	$2Q^2(\mathrm{OAl_2}) + 2A^2(\mathrm{OH})_2/2Q^2(\mathrm{O})(\mathrm{OAl}) + 2A^2(\mathrm{OH})(\mathrm{OSi})$	433.8441	0.140
	$Q^2(\mathrm{OAl_2}) + Q^2(\mathrm{O})(\mathrm{OAl_2}) + 2A^2(\mathrm{OH})_2/Q^2(\mathrm{O})(\mathrm{OAl}) + Q^2(\mathrm{OAl}) + 2A^2(\mathrm{OH})(\mathrm{OSi})$	433.6330	0.141
(112)	$2Q^1(\mathrm{O})(\mathrm{OAl_2}) + 2A^4(\mathrm{OH})/2Q^1(\mathrm{O})(\mathrm{OAl}) + 2A^4(\mathrm{OSi})$	436.1347	0.095
	$2Q^2(\mathrm{OAl}) + 2A^4(\mathrm{OH})(\mathrm{OSi})/2Q^2(\mathrm{O})(\mathrm{OAl_2}) + 2A^4$	437.0017	0.092

TABLE 3: Surface Energies and Sites in Periodic Spin-Polarized Calculations of Quartz

type	sites on complementary surfaces	$-E_{\mathrm{slab}}{}^{\alpha-\beta=0}$ [eV]	$\gamma_{\mathrm{fr}}{}^{\alpha-\beta=0}$ [eV·Å^{-2}]	$-E_{\mathrm{slab}}{}^{\alpha-\beta=2}$ [eV]	$\gamma_{\mathrm{fr}}{}^{\alpha-\beta=2}$ [eV·Å^{-2}]
(101)	$Q^3(\mathrm{O}) + Q^3/Q^3(\mathrm{O}) + Q^3$	275.1190	0.161	275.247	0.159
(112)	$2Q^3(\mathrm{O}) + 2Q^3/2Q^3(\mathrm{O}) + 2Q^3$	no convergence			
(001)	$Q^2(\mathrm{O})/Q^2(\mathrm{O})$	134.7799	0.193	no data	
(102)	$Q^2(\mathrm{O}) + Q^3 + Q^3(\mathrm{O})/Q^2(\mathrm{O}) + Q^3(\mathrm{O}) + Q^3$	265.8310	0.198	no convergence	
(100)	$Q^2(\mathrm{O})/Q^3(\mathrm{O}) + Q^3$	276.7196	0.177	276.0497	0.188
(111)	$Q^2(\mathrm{O}) + Q^3(\mathrm{O}) + Q^3/Q^2(\mathrm{O}) + Q^3(\mathrm{O}) + Q^3$	265.7812	0.195	no convergence	
(110)	$2Q^2(\mathrm{O})/Q^2 + 2Q^3(\mathrm{O})$	267.7107	0.195	no data	
	$2Q^2(\mathrm{O})/Q^2(\mathrm{O}) + Q^3(\mathrm{O}) + Q^3$	267.5862	0.196	267.3513	0.198

splitting occurs. The mechanism of covalent bond splitting is either homolytic or heterolytic.[20] In the homolytic mechanism, the electron density of molecular orbital splits evenly between the separating atoms, resulting in two neutral fragments of the crystal that contain surface radicals.[34] In the heterolytic mechanism, the bonding electron pair is transferred onto a molecular orbital of either of the fragments resulting in a fragment that becomes negatively charged and a complementary fragment that becomes charged positively.

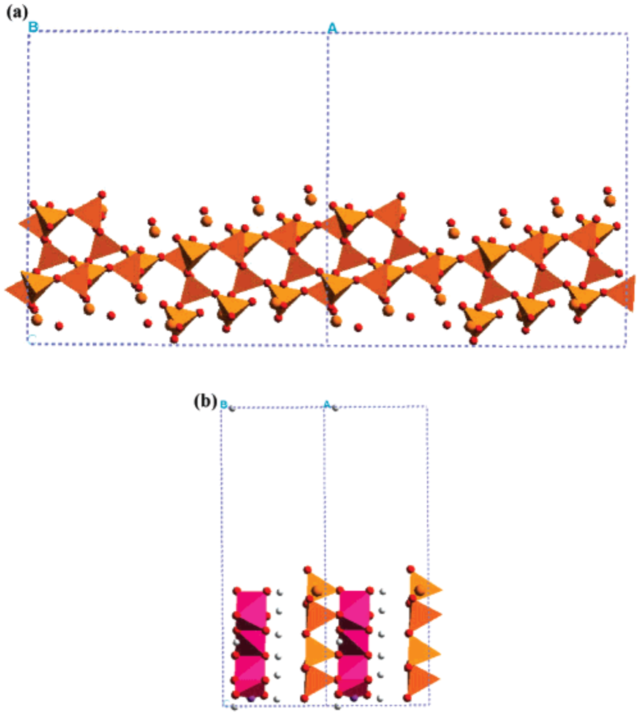

Figure 3. Polyhedral representation of (a) the (511) surface of quartz and (b) the (010) surfaces of kaolinite. The viewing direction is along the surface of the slab, i.e., the normal to the surface is perpendicular to the bottom of the page.

A combinatorial explosion prevents the exhaustive analysis of each possible combination of ruptured sites emerging at the surface. To get an idea of the magnitude of the expected effect due to homo- or heterolytic cleavage, we carried out test spin-polarized calculations on several low-index surfaces. Since computational complexity rapidly increases with increasing complexity of the surface, our calculations were limited to low-index surfaces. No substantial energy differences between the homolytic and heterolytic cleavage were found. We performed spin-polarized calculations with equal numbers of α- and β-spin electrons [$N(\alpha) = N(\beta)$] and with a number of α-spin electrons exceeding the number of β-spin electrons by two [$N(\alpha) - N(\beta) = 2$] per supercell of the slab (Table 3). In the first case, the electronic convergence was achieved for all investigated surfaces except for the (112) surface, while in the second case, the electronic convergence was achieved for only (101), (100), and (110) surfaces. Conceivably, the optimization procedure experienced difficulties in finding a local minimum electronic configuration in spin-polarized calculations due to an increased number of electronic degrees of freedom.

In 9 out of 10 cases the specific surface energy differences between results of spin-polarized and spin-paired calculations was less than 2% (Tables 1 and 3). In the case of the (100) surface, the specific surface energy obtained in spin-polarized calculations was 6% higher than that in the spin-paired case. Since spin-polarized calculations were less stable but more computationally demanding, and their results seemingly did not impact conclusions drawn from spin-paired calculations, spin-polarized calculations on the surfaces represented by large supercells were not performed. Further discussion is limited to only spin-paired calculations, which imply the heterolytic bond splitting mechanism.

If the original molecule is neutral, the heterolytic mechanism creates ionized species on the fragments of the broken bond. To this end it is similar to ionic bond splitting. Therefore, we may expect that the rules of cleavage surface formation on covalent and ionic crystals are similar. It is known that ionic

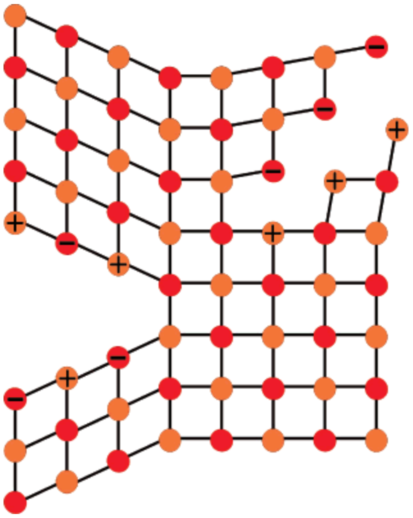

Figure 4. A two-dimensional schematic representation of a crystal cleaved by heterolytic mechanism. The surfaces created by the left-hand-side crack are likely to exist because each of them carries a pattern of alternating charges. The surfaces created by the right-hand-side crack are uniformly charged. Therefore, these surfaces are not expected to develop.

crystals do not cleave on crystal planes which result in an excessive noncompensated charge on the fractured surface.[35] Instead, the ionic crystals cleave along planes which satisfy the crystal-plane neutrality condition, which can be achieved in a chess-like configuration of charges of alternating polarity (Figure 4). In Table 1 we investigate if this principle of ionic crystal cleavage applies to quartz. Using tentative distributions of sites on idealized complementary singular surfaces of quartz, we conclude that in all cases the cuts with a more uniform distribution of surface sites at the opposite sides of the cleavage plane are associated with lower surface energy. However, the excess of surface energy on uneven cuts does vary. The variation is due, in part, to different concentrations of anionic siloxy and cationic silyl groups. The observed spread of surface energies ranges from 0.005 eV·Å^{-2} (or 8.6 kJ per mol of silyl/siloxy sites) for the {112} and {22} correlated forms to 0.025 eV·Å^{-2} (or 41.8 kJ per mol of silyl/siloxy sites) for the {101} form. These values correspond to approximately 2−15% of the total specific energies of the surfaces, which indicates that charged surfaces on quartz may be created, especially if an extreme external stress is applied. This condition is common in mining and construction, which often rely on a high-energy technology of material comminution.

Low surface energies are also obtained for cuts with a more uniform distribution of oxygen atoms among the ruptured geminal surface sites favoring neutral sites over the charged ones (the neutral sites emerge when two oxygen atoms of the same silica unit split evenly between the two sides of the crack). This type of surface stabilization ranged from an almost negligible amount for the (110) surface to 0.036 eV·Å^{-2} for the (001) surface.

In general, correlated crystal forms are expected to have distinct energies because of the differences in surface−surface and surface−bulk intersite interactions. The analysis of Table 1 in terms of crystal forms suggests that the variation of surface energy between correlated crystal forms of quartz was not large. For unrelaxed surfaces, we obtained energy differences that ranged from zero for the {112} and {$2\bar{1}2$} correlated forms to 0.003 eV·Å^{-2} for the {101} and {011} forms. Relaxed surfaces of correlated forms are known to have distinct probabilities of occurrence suggestive of differences in surface energies. For example, in natural crystals the {101} form is predominantly observed among the {101} and {011} correlated forms.[10]

The crystal form of first-order hexagonal prism deserves special attention. Cleavage along the (100) plane yields two surfaces, one of which is exclusively covered with single silanol groups, the (100)^{S} surface, and another with exclusively geminal silanol groups, the (100)^{G} surface. Because of the crucial physiological importance of these distinctions[36] we further investigated these complementary surfaces by preparing and analyzing noncomplementary slabs terminated on both ends with the same type of surface. We found that the (100)^{S} surface had a higher unrelaxed surface energy (0.196 eV·Å^{-2}) than the (100)^{G} surface (0.161 eV·Å^{-2}). This result agrees well with earlier self-consistent tight-binding calculations,[5] which showed that the (100)^{S} surface has a higher energy than the unrelaxed (001) surface. On the other hand, after relaxation the energy of the (100)^{S} surface becomes lower than the energy of the (100)^{G} surface (0.104 eV·Å^{-2} vs 0.117 eV·Å^{-2}).[21] Thus, we expect that geologically aging particles will tend to refacet with surfaces exclusively covered with single silanol groups, provided appropriate surface reconstruction conditions are met.

Overall, our calculations indicate that the specific surface energies of facetted quartz must be confined within a capped range of energies. The highest obtained value was 0.229 eV·Å^{-2}. It was calculated by using a relatively simple basal (001) cut (Table 1). Although we do not have a rigorous proof that this number represents the upper bound on the energy, our calculations on more complex surfaces up to (511) do not suggest an association between the increasing surface complexity and energy of the cut. In fact, some of our data[9] relate the minimum specific surface energy of the cut to the density of silanol groups on its surface, and since the basal cut is one of the most densely populated, we may expect that its energies provide a reasonable approximation to the upper bound of specific surface energies of cleaved quartz.

The calculated minimum unrelaxed surface energies of quartz ranged from 0.161 to 0.200 eV·Å^{-2}. On one hand, these variations can be considered significant, because several types of surfaces with “high-energy” surface sites, e.g. 2Q^3(O)/2Q^3 on {101}, 2Q^3(O)/2Q^3 on {011}, etc., were encompassed within this range, but on the other, the range may be considered as relatively narrow, because *all* surfaces described in Table 1 are found on the conchoidal fracture of quartz with given frequencies.[11] Therefore, a possibility of formation in the processes of mechanical comminution of at least some high-energy surface sites, which are reported in Tables 1 and 3, may not be excluded. From statistical−mechanical considerations, we may expect that the most abundant fracture of quartz will develop over the minimum free energy interface, i.e., the interface made up of singular surfaces with the lowest excess free energy of surface sites.[9] Using this principle, the average surface energy of the conchoidal fracture of quartz amounts to 0.187 eV·Å^{-2} or 3.0 J/m^2.

The calculated surface energies favorably agree with results of tensile stress measurements. On the basis of a compilation of seven references with numbers ranging from 0.28 to 11.5 J/m^2, Parks has suggested that the gas-phase energy of dry pristine quartz surface must be above 2.0 J/m^2.[37] Another estimate could be analytically derived from macroscopic considerations. Assuming in the Orowan equation[38] the irreversible fracture deformation distance of Si−O bonds as 2 Å and the theoretical strength of the ideal brittle quartz material as ∼35 GPa and using 76.5 and 97.2 GPa as Young’s moduli,[39] we obtain 3.2 and 2.5 J/m^2 for perpendicular and parallel idealized γ_{fr}, respectively. This range is in remarkable compliance with surface energies reported in Table 1.

Although the surface energies presented in Tables 1 and 3 are large on the per mole basis (270−490 kJ/mol), the mechanical work associated with creation of these surfaces is quite modest. Taking into account that the total surface area of typical respirable quartz dust varies from approximately 0.3 to 4.0 m^2/g[40,41] and neglecting dissipation of energy in the form of heat, sound, irreversible elastic deformation, piezoelectric effects, and other less prominent dissipation regimes, the minimum work required to create the surface of 1 g of respirable quartz participles would amount to 1−12 J. This is an absolutely negligible quantity compared to the energetics of machining and blasting processes used in mining and construction. As a consequence we expect that any type of "high-energy" surface analyzed in the present work may be present on particles produced in mining and construction. In particular, a static macroscopic noncompensated electrostatic charge on the surfaces of cleaved quartz may be created. Charging of the cleaved quartz surface is observed experimentally and is acknowledged as an important factor in the processes of agglomeration of utrafine quartz particles,[42] and in piezoelectric effects in respirable quartz dust.[43] Surface charging due to heterolytic cleavage may be directly related to the observed higher toxicity of freshly fractured quartz as compared to retained (but not "geologically aged") samples.[44,45] Charged silica particles are known to promote the activity of collagenase, a precursor of silicosis.[46] The chemical and toxicological consequences of surface charging were recently analyzed in detail in connection with piezoelectric effects on crystalline silica.[43] It was concluded that surface charging induces rapid adsorption of atmospheric components with further release of highly reactive silylperoxide, ozonide, and superoxide free radicals. The presence of large amounts of free radicals on freshly cleaved quartz surface is measurable by electron paramagnetic resonance.[47−51] This type of quartz surface activity is associated with acute forms of silicosis, to which workers engaged in sandblasting, drilling, or grinding are at risk.[45]

Kaolinite Surfaces. Similar to quartz, pristine kaolinite surfaces can accommodate several types of silanol sites. In addition, kaolinite surfaces can differ in the aluminol site distributions and in patterns of hydrogen-bond networks due to the presence of mobile protons of aluminol hydroxyl groups. Therefore, more factors contribute to the surface energy of kaolinite than quartz. In our calculations, a more uniform distribution of silyl/siloxy surface sites between complementary surfaces on {100} and {111} forms did not result in lower surface energies (Table 2). This observation is related to the interactions between silica and alumina sites. On the other hand, a more even distribution of oxygen atoms between noncharged sites did result in lower surface energies. For example, the low-energy cuts of the (101) and (011) surfaces were built by transferring an oxygen atom of the siladioxyrane site to a silyl site of the other complementary surface. As a result, the latter side of the slab has alternating silyl and siloxy sites. As expected, cuts with geminal (silanone) sites are higher in energy than those with single (silyl/siloxy) sites. This was observed by investigation of the (010) and (110) surfaces.

The formation of the basal (001) kaolinite surface did not involve any change in the coordination numbers of surface atoms. Thus, the (001) surface energy was largely the energy of hydrogen-bond interactions between silica/alumina bilayers. This unrelaxed surface had the highest concentration of uncoordinated hydrogen atoms of interbilayer aluminol groups, which resulted in a very low surface energy and thus explained the prevalence of this form as a natural habit of kaolinite crystals. We estimated its specific surface energy at 0.0072 $eV \cdot Å^{-2}$ or 132.3 kJ/mol using data for relaxed structures of both bulk kaolinite and an isolated bilayer. (This compares favorably with a previously reported[6] value of 116.7 kJ/mol. It is also likely to underestimate surface energy due to poor representation of dispersion interactions by DFT methods.[52]) The unrelaxed (001) surface energy was 0.017 $eV \cdot Å^{-2}$ (Table 2). Therefore, the energy of the hydrogen-bond network relaxation can be as high as 0.01 $eV \cdot Å^{-2}$.

The lowest unrelaxed pristine surface energy among the surfaces with altered coordination of surface atoms was found for the {112} form (Table 2), and this form had the lowest concentration of broken Al−O and Si−O bonds. The lowest energy cut for this surface can be described as a terrace of the (110) and (001) bilayer surfaces. Therefore, the (112) surface had the second highest concentration of uncoordinated hydrogen atoms of intra- and interbilayer aluminol groups and its surface energy was intermediate between those of the (110) and (001) surfaces. The (100) surface had a high concentration of broken Si−O and Al−O bonds and the highest surface energy. Surfaces of the {010} and {110} forms were found to have similar energies, and they were lower than the energy of the {100} form. It is conceivable that the reconstructed {010} and {110} forms also have low surface energy due to their prominence in the natural habit of kaolinite crystals.[17]

Overall, the calculated unrelaxed minimum surface energies of primitive kaolinite cuts were found to range between 0.017 and 0.158 $eV \cdot Å^{-2}$, with two surfaces, (001) and (112), significantly deviating toward the lower end of the energy distribution. Excluding these two surfaces, which are covered by relatively inert siloxane bridges, the energies of all other kaolinite surfaces were found to be confined within the 0.042 $eV \cdot Å^{-2}$ range. The energy gap between this band of energies and the energy of the minimum-energy surface (which is the basal surface) was approximately 0.1 $eV \cdot Å^{-2}$, which is more than twice greater than the width of the energy band. This clearly differentiates the basal cut of kaolinite from the pool of other studied surfaces, and it is coherent with the basal cut being a distinguished cleavage plane in kaolinite.[14] This differentiates kaolinite from quartz, for which no deviants from the main surface energy band were identified.

Conclusions

This study described the most probable cuts of common unrelaxed surfaces of quartz and kaolinite. Periodic density functional theory calculations were employed to calculate their surface energies. Unrelaxed surface energies, pertinent to the cleavage frequency, were lowered by more even distribution of charged surface sites and oxygen atoms between the complementary surfaces of the cut. We found that in all studied cases the energies of kaolinite surfaces were lower than the surface energies of quartz, which we view as a consequence of the lower density of surface sites on kaolinite. The lowest specific surface energies were in the range from 0.161 to 0.200 $eV \cdot Å^{-2}$ for quartz low-index surfaces and from 0.017 to 0.158 $eV \cdot Å^{-2}$ for kaolinite. However, the energy ranges spanned by most of the kaolinite and quartz surfaces were similar (compare 0.042 $eV \cdot Å^{-2}$ for kaolinite and 0.038 $eV \cdot Å^{-2}$ for quartz). The only exceptions were the (001) surface of kaolinite, which significantly deviated from the major band of surface energies, and the (112) surface, which embeds terraces of the (001) surface. Therefore, we expect that in mechanically fractured particulate the frequency of basal surfaces may significantly prevail over other types of surfaces in kaolinite, whereas in quartz the prevalence effect would be less profound. We also expect that some quantities of many, if not all, types of studied surfaces may be present in quartz particulate obtained by high-energy comminution processes, because on a macroscopic scale the energetics of particulate surface is negligible compared with the comminuting energies involved. Relative enrichment with high-energy surfaces of mechanically comminuted quartz may be directly connected to the observed high toxicity[1,2,42,45,51] of respirable crystalline silica particulate. At present, exposures to respirable dust containing crystalline silica are regulated by permissible exposure limits (PELs) for the construction[53] and general[54] industry. Both of them are based on particle count. Subject to experimental validation, our hypothesis permits further differentiation and improvement of these and related occupational health standards based on surface characterization of respirable particulate material.

Disclaimer: The findings and conclusions in this report are those of the authors and do not necessarily represent the views of the authors' parent institutions.

References and Notes

(1) *IARC Monographs on the evaluation of the carcinogenic risk of chemical to humans: silica, some silicates, coal dust and para-aramid fibrils*; World Health Organization (distributor): Lyon, France, 1997; Vol. 68.

(2) Nash, T.; Alison, A. C.; Harington, J. S. *Nature* **1966**, *211*, 259.

(3) Koretsky, C. M.; Sverjensky, D. A.; Sahai, N. *Am. J. Sci.* **1998**, *298*, 349.

(4) Demuth, Th.; Jeanvoine, Y.; Hafner, J.; Ángyán, J. G. *J. Phys. Condens. Matter* **1999**, *11*, 3833.

(5) Goniakowski, J.; Noguera, C. *Surf. Sci.* **1994**, *319*, 68.

(6) Benco, L.; Tunega, D.; Hafner, J.; Lischka, H. *Am. Miner.* **2001**, *86*, 1057.

(7) Benco, L.; Tunega, D.; Hafner, J.; Lischka, H. *J. Phys. Chem. B* **2001**, *105*, 10812.

(8) Tunega, D.; Benco, L.; Haberhauer, G.; Gerzabek, M. H.; Lischka, H. *J. Phys. Chem. B* **2002**, *106*, 11515.

(9) Murashov, V. V.; Demchuk, E. *Surf. Sci.* Submitted for publication.

(10) Frondel, C. *System of Mineralogy of Dana*, 7th ed.; Silica Minerals, Vol 3; New York: John Wiley and Sons: New York, 1962.

(11) Bloss, F. B.; Gibbs, G. V. *Am. Miner.* **1963**, *48*, 821.

(12) The crystal form encompasses a set of crystallographic faces, which have distinct Miller indices, but which are connected via elements of symmetry and, therefore, equivalent.

(13) Bish, D. L. *Clays Clay Miner.* **1993**, *41*, 738.

(14) *Handbook of Mineralogy*; Anthony, J. W., Bideaux, R. A., Bladh, K. W., Nichols, M. C., Eds.; Silica, Silicates, Vol. II; Mineral Data Publishing: Tucson, AZ,1995.

(15) Zoltai, T.; Stout, J. H. *Mineralogy*: *Concepts and Principles*; Burgess Publ. Co: Minneapolis, MN, 1984; p 505.

(16) Shoval, S.; Yariv, S.; Michaelian, K. H.; Boudeulle, M.; Panczer, G. *Clays Clay Miner.* **2002**, *50*, 56.

(17) Sweegers, C.; van Enchevort, W. J. P.; Meekes, H.; Bennema, P.; Hiralal, I. D. K.; Rijkeboer, A. *J. Cryst. Growth* **1999**, *197*, 244.

(18) Sweegers, C. On the diversity of gibbsite crystal shapes, defects and kinetics, Thesis; Katholieke Universiteit Nijmegen, Nijmegen, The Netherlands, 2001.

(19) Peskleway, C. D.; Henderson, G. S.; Wicks, F. J. *Am. Mineral.* **2003**, *88*, 18.

(20) Murashov, V. V. *J. Mol. Struct.* **2003**, *650*, 141.

(21) Murashov, V. V. *J. Phys. Chem B.* **2005**, *109*, 4144.

(22) D'Souza, A. S.; Pantano, C. G. *J. Am. Ceram. Soc.* **1999**, *82*, 1289.

(23) Blöchl, P.; Jepsen, O.; Andersen, O. K. *Phys. Rev. B* **1994**, *49*, 16223.

(24) Vanderbilt, D. *Phys. Rev. B* **1990**, *41*, 7892.

(25) Kresse, G.; Hafner, J. *J. Phys.*: *Condens. Matter* **1994**, *6*, 8245.

(26) Kresse, G.; Hafner, J. *Phys. Rev. B* **1993**, *48*, 13115. Kresse, G.; Hafner, J. *Phys. Rev. B* **1994**, *49*, 14251.

(27) Kresse, G.; Furthmüller, J. *Comput. Mater. Sci.* **1996**, 6, 15. Kresse, G.; Furthmüller, J. *Phys. Rev. B* **1996**, *54*, 11169.

(28) Perdew, J. P.; Chevary, J. A.; Vosko, S. H.; Jackson, K. A.; Pedersen, M. R.; Singh, D. J.; Fiolhais, C. *Phys. Rev. B* **1992**, *46*, 6671.

(29) Monkhorst, H. J.; Pack, J. D. *Phys. Rev. B* **1976**, *13*, 5188.

(30) Rignanese, G.-M.; De Vita, A.; Charlier, J.-C.; Gonze, X.; Car, R. *Phys. Rev. B* **2000**, *61*, 13250.

(31) Jepsen, O.; Andersen, O. K. *Solid State Commun.* **1991**, *9*, 1763.

(32) Levien, L.; Prewitt, C. T.; Weidner, D. J. *Am. Miner.* **1980**, *65*, 920.

(33) Young, R. A.; Hewat, A. W. *Clays Clay Miner.* **1988**, *36*, 225.

(34) Hochstrasser, G.; Antonini, J. F. *Surf. Sci.* **1972**, *32*, 644.

(35) Schultz, R. A.; Jensen, M. C.; Bradt, R. C. *Int. J. Fracture* **1994**, *65*, 291.

(36) Murashov, V. V.; Harper, M.; Demchuk, E. *Env. Health Persp.* Submitted for publication.

(37) Parks, G. A. *J. Geophys. Res.* **1984**, *89*, 3997.

(38) Shelby, J. E. *Introduction to Glass Science and Technology*; RSC: Cambridge, UK, 1997; p 185.

(39) *Handbook of Infrared Optical Materials*; Klocek, P., Ed.; Marcel Dekker: New York, 1991; p 346.

(40) Yabuta, J.; Ohta, H. *Ind. Health* **2003**, *41*, 249.

(41) Gao, N.; Keane, M. J.; Ong, T.; Ye, J.; Miller, W. E.; Wallace, W. E. *Toxicol. Appl. Pharmacol.* **2001**, *175*, 217.

(42) Fubini, B. Health effect of silica. In *The surface properties of silicas*; Legrand, A. P., Ed.; John Wiley: Chichester, UK, 1998; pp 415−464.

(43) Williamson, B. J.; Pastiro, S.; Cressey, G. *Atmos. Environ.* **2001**, *35*, 3539.

(44) Göethe, C. J.; Lidstrom, L.; Swensson, A. *Med. Lav.* **1971**, *62*, 375.

(45) Vallyathan, V.; Castranova, V.; Pack, D.; Leonard, S.; Shumaker, J.; Hubbs, A. F.; Shoemaker, D. A.; Ramsay, D. M.; Pretty, J. R.; Mclaurin, J. L.; Khan, A.; Teass, A. *Am. J. Respir. Crit. Care Med.* **1995**, *152*, 1003.

(46) Bagchi, N. *Brit. J. Ind. Med.* **1992**, *49*, 163.

(47) Costa, D.; Fubini, B.; Giamello, E.; Volante, M. *Can. J. Chem.* **1991**, *69*, 1427.

(48) Fubini, B.; Bolis, V.; Giamello, E. *Inorg. Chim. Acta Bioinorg. Chem.* **1987**, *138*, 193.

(49) Fubini, B.; Giamello, E.; Volante, M.; Bolis, V. *Toxicol. Ind. Health* **1990**, *6*, 571.

(50) Ratdzig, V. A.; Bystrikov, A. V. *Kinet. Katal.* **1978**, *19*, 713.

(51) Shi, X. L.; Dalal, N. S.; Vallyathan, V. *J. Toxicol. Environ. Health* **1988**, *25*, 237.

(52) Xu, X.; Goddard, W. A., III *J. Phys. Chem. A* **2004**, *108*, 2305.

(53) Federal Register, *Safety and Health Regulations for Construction*; OSHA: Washington, DC; 29 CFR 1926.55.

(54) Federal Register, *Occupational Safety and Health Standards*; OSHA: Washington, DC; 29 CFR 1910.1000.